Efficient Free Triplet Generation Follows Singlet Fission in Diketo-pyrrolopyrrole Polymorphs with Goldilocks Coupling

Andrew M. Levine[1,2,3], **Guiying He**[4,5], **Guanhong Bu**[6], **Pablo Ramos**[7], **Fanglue Wu**[8], **Aisha Soliman**[1,2], **Jacqueline Serrano**[1,2], **Dorian Pietraru**[1,2], **Christopher Chan**[1], **James D. Batteas**[8,9], **Marta Kowalczyk**[7,10], **Seogjoo J. Jang**[3,5,7], **Brent L. Nannenga**[6], **Matthew Y. Sfeir**[3,4,5], **Esther H. R. Tsai**[11], **Adam B. Braunschweig**[1,2,3]

[1]Nanoscience Initiative, Advanced Science Research Center, Graduate Center, City University of New York, 85 St. Nicholas Terrace, New York, NY 10031, USA

[2]Department of Chemistry, Hunter College, 695 Park Avenue, New York, NY 10065, USA

[3]Ph.D. Program in Chemistry, The Graduate Center of the City University of New York, New York, NY 10016, USA

[4]Photonics Initiative, Advanced Science Research Center, Graduate Center, City University of New York, 85 St. Nicholas Terrace, New York, NY 10031, USA

[5]Department of Physics, Graduate Center, City University of New York, New York, NY 10016, USA

[6]Chemical Engineering, School for Engineering of Matter, Transport, and Energy, Arizona State University, Tempe, AZ 85287, USA

[7]Department of Chemistry and Biochemistry, Queens College, City University of New York, 65-30 Kissena Boulevard, Queens, New York 11367, United States

[8]Department of Materials Science and Engineering, Texas A&M University, College Station, Texas 77843, USA.

[9]Department of Chemistry, Texas A&M University, College Station, Texas 77843, USA.

[10]Department of Natural Sciences, LaGuardia Community College, City University of New York, New York, NY 11101, USA.

[11]Center for Functional Nanomaterials, Brookhaven National Laboratory, Upton, NY 11973, USA.

Abstract

Microcrystal electron diffraction, grazing incidence wide-angle scattering, and UV-Vis spectroscopy were used to determine the unit cell structure and the relative composition of dimethylated diketopyrrolopyrrole (MeDPP) H- and J-polymorphs within thin films subjected to vapor solvent annealing (VSA) for different times. Electronic structure and excited state deactivation pathways of the different polymorphs were examined by transient absorption spectroscopy, conductive probe atomic force microscopy, and molecular modeling. We find VSA initially converts amorphous films into mixtures of H- and J-polymorphs and promotes further conversion from H to J with longer VSA times. Though both polymorphs exhibit efficient SF to form coupled triplets, free triplet yields are higher in J-polymorph films compared to mixed films because coupling in J-aggregates is lower, and, in turn, more favorable for triplet decoupling.

Graphical Abstract

Goldilocks Coupling

amorphous   *H*-aggregate   *J*-aggregate

too weak   *too strong*   *just right*

SF Free Triplet Yield
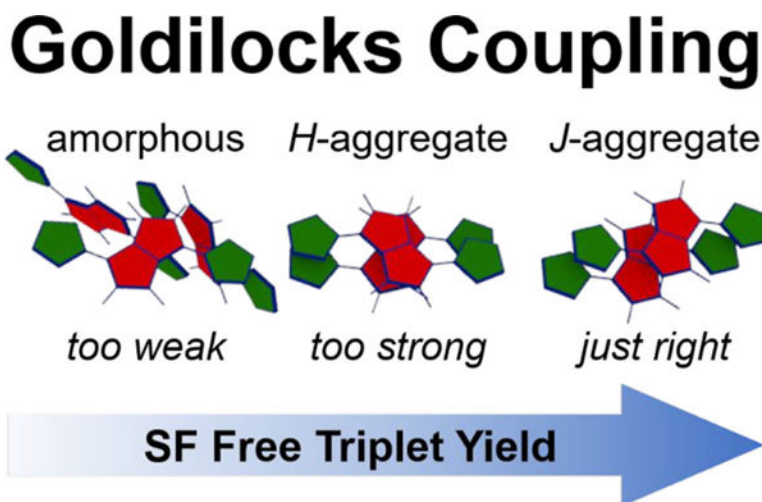
Introduction

Organic dyes that undergo singlet fission (SF) can overcome the Shockley-Queisser efficiency limit[1] imposed on single band gap photovoltaics by ~10% when adopted as sensitizers, and as a consequence are the subject of substantial current research.[2–3] SF is a multiexciton process where photoexcitation of electronically coupled chromophores generates a singlet exciton S_1 that undergoes a spin-allowed relaxation process to a triplet pair multiexciton state $^1(T_1T_1)$, which can subsequently decouple to form free triplets 2 x (T_1) (Eq. 1).[4] Following decoupling, these triplets can be harvested via charge/exciton transfer[5–7] or used for photocatalysis[8].

$$S_1 \leftrightarrow (T_1T_1) \leftrightarrow 2 \text{ x } (T_1)$$ Eq. 1

Despite the potential benefits of SF chromophores, their incorporation into devices has been hampered by several unresolved challenges and an incomplete understanding of the factors that lead to efficient (T_1) formation. Each step in SF is sensitively dependent on the detailed chemical and electronic characteristics of the system, including the molecular orbitals involved in spin-orbital coupling, singlet and triplet exciton energies, and chromophore

packing morphology. As such, maximizing (T_1) yields and lifetimes requires understanding both the energetic and geometric factors that affect triplet yield. Generally, dimeric dyes are prepared to control geometry and their photophysics are studied in solution. These studies confirmed the expected trend that the decrease in the electronic coupling, V_{ST}, between S_1 and $^1(T_1T_1)$ reduces $^1(T_1T_1)$ yields. However, too strong V_{ST} mitigates subsequent decoupling into (T_1)[9–17]. This implies that there is an optimal, 'Goldilocks coupling' – not too strong and not too weak – that maximizes (T_1) yield for a particular dye. Drawbacks of this approach, however, are that dye structure and energetics of molecular orbitals are both changing, making it difficult to isolate the effect of V_{ST} from other effects, especially when actual molecular structures differ significantly from computational ones optimized for the ground electronic state. In addition, to investigate how molecular arrangement affects excited state deactivation, only well-characterized molecular packing geometries should vary, thereby providing a means to isolate coupling effects. As such, polymorphic SF dyes are favorable candidates for investigating these questions because the effects of V_{ST}, arising from different packing arrangements, can be separated more easily from those that arise from alterations in electronic states and molecular structure. The few studies of SF in polymorphic materials, such as tetracene[18] and pentacene[19], have revealed that the effects of polymorphism on SF may not agree with theory or computational results, and predicting whether a system undergoes SF via charge transfer (mediated) or a superexchange mechanism (direct) is still a major challenge[20]. Further, it is also difficult to predict the effect of polymorphism on SF yields as in the case with 1,3-diphenylisobenzofuran polymorphs,[21] where yields differ by orders of magnitude. Because of difficulty in growing sizeable single crystals of each polymorph for X-ray diffraction analysis, packing information remained elusive in most studies.

In an important series of studies for understanding the effect of coupling on SF, Wasielewski[22] and Michl[23] investigated how substituents on the nitrogens of diketopyrrolopyrroles (DPPs) influence SF yield. DPPs are an attractive class of chromophores for the active layers of photovoltaics[24–26] because they are stable in ambient conditions, have relatively high extinction coefficients, and have highly tunable structures that permit control of solubility, molecular packing in films, electronic energy levels, and, importantly, they undergo SF because triplet energies are roughly half their singlet state value.[2, 27–33] One of the derivatives used in both studies, di-*N*-methylated DPP (MeDPP), exhibited nearly 200% (T_1T_1) yield, but only after vapor solvent annealing (VSA). Wasielewski reports from grazing incidence wide-angle X-ray scattering (GIWAXS) data that "The unannealed film of MeDPP has an additional peak at 9.7° compared to the calculated powder pattern, which disappears upon solvent vapor annealing. This peak most likely results from a polymorph that is then converted to the single crystal structure upon annealing"[22], but the additional polymorph was unsolved and its SF behavior undetermined. Identifying and directly comparing the structures and photophysical data of the solved and unsolved polymorphs could provide invaluable insight into how packing geometry and coupling affect yields in each step of the SF process. Here we employ microcrystal electron-diffraction (MicroED) to solve both MeDPP polymorphs, including the polymorph that occurs prior to VSA, and show that the elusive MeDPP polymorph has dominant characteristics of an *H*-aggregate. VSA converts both amorphous and *H*-aggregate MeDPP

into *J*-aggregates. The relative proportions of *H*- and *J*-aggregates in films were determined using GIWAXS, UV-vis spectroscopy, and scanning probe methods. Transient absorption (TA) and molecular modeling were used to quantify SF efficiencies and coupling constants, V_{ST}, respectively. We found that both *H*- and *J*-aggregates undergo efficient SF to form (T_1T_1), but *H*-aggregates yield fewer (T_1) likely because of a higher V_{ST}.

Methods

MicroED uses a TEM to determine crystal structures from the diffraction of crystallites with micrometer or nanometer edge lengths, and is advantageous because it circumvents the need for the large crystals required in conventional single-crystal X-ray analysis.[34–37] We recently validated the utility of this method for determining the crystal structures of organic semiconductors, including those containing DPP groups,[38] and here we use MicroED to show that two distinct polymorphs exist in the MeDPP films and determine the unit-cell structures of both. TEM grids were prepared by drop-casting a 10 mM solution of MeDPP in PhMe onto continuous carbon grids. Some grids were investigated as-deposited while others were exposed to CH_2Cl_2 vapor for 1 hour. The unannealed grids possess small crystallites of two distinct polymorphs (Figure S2), whereas the annealed sample possessed only a single polymorph, which was also found in the unannealed sample. The unit cells of both polymorphs (Figure 1A) were solved by direct methods from their MicroED diffraction patterns to reveal *H*-type and *J*-type aggregates, the latter of which is exclusively present on the annealed grids and matches the previously reported structures[22, 39]. Both unit cells have herringbone geometries possessing two molecules of MeDPP in a P2$_1$/n space group, though conversion from *H*- to *J*-aggregate requires one of the two molecules in the antiparallel-stacked *H*-aggregate unit cell to convert into a parallel, slip-stacked geometry. The unit cell for *J*-aggregates is composed of slip-stacked MeDPP molecules with $\pi \cdots \pi$ stacking distances of 3.3 Å and centroid offsets of 3.2 Å and 1.6 Å for x and y, respectively. The antiparallel *H*-aggregates have $\pi \cdots \pi$ stacking distances of 3.4 Å and centroid offsets of 0.51 Å and 0.46 Å for x and y, respectively.

MeDPP films were prepared, and they were studied by GIWAXS with different VSA times to monitor the dynamics of interconversion of the polymorphs within the films. MeDPP thin films (216 ± 18 nm) were prepared by thermal evaporation at a rate of 0.5 Å·s^{-1} onto clean glass slides, and VSA was carried out by exposing the films to CH_2Cl_2 vapor for 1 to 60 minutes. GIWAXS 2D integration reveals the disappearance of a *q*-space signal near 0.7 Å^{-1} (Figure 1B & S3) with increasing VSA time, indicating a conversion of one polymorph into another. By comparing the calculated powder pattern from the MicroED solved crystal structures to the GIWAXS 1D integrated intensity *vs. q*,[38] the fading intensities are assigned to the MeDPP *H*-aggregate and remaining intensities to the *J*-aggregate (Figure 1C). Further, we can assign unit-cell orientation with respect to the substrate normal (Figure 1D), and both aggregates have a preferred orientation with respect to the surface.

UV-Vis spectroscopy was performed to estimate composition on the thin films, which progressively turned from purple to pink with increasing VSA times (0 – 60 min) (Figure 2A). MeDPP films were exposed to CH_2Cl_2 for different times, and UV-Vis spectra were taken at each time point (Figure 2B). Following ~50 min of annealing, the film color stopped

changing, indicating that the film had reached an equilibrium structure. The peaks, λ_1 and λ_2, red-shifted 10 and 11 nm, respectively, in going from 1 min to 60 min VSA time. Red shifting and increasing λ_1:λ_2 peak intensities have been correlated previously to the formation of *J*-aggregates.[40–41] With the exception of the spectra for the film taken prior to annealing, all spectra pass through isosbestic points, indicating gradual changes that shift oscillator strengths, which are likely from gradual shifting in the structure from *H*- to *J*-aggregates. The lower intensity of the spectrum taken prior to annealing is attributed to the presence of a third component – amorphous MeDPP – in the film. This interpretation is supported by variable temperature UV-Vis studies on MeDPP solutions (Figure S6). As dilute MeDPP solutions in PhMe are heated, the extinction coefficients decrease, and the maxima shift hypsochromically. These spectral changes have been previously correlated with DPP disaggregation[42] thus further confirming that the low intensity of the unannealed film is the result of the presence of amorphous MeDPP, which disappears immediately upon beginning the VSA process. These data are further supported by conductive probe atomic force microscopy (CP-AFM) and scanning tunneling microscopy/scanning tunneling spectroscopy (STM/STS). Samples were prepared by briefly thermally evaporating MeDPP at a rate of 0.5 Å·s^{-1} onto Au (111) surfaces, and some were treated with 60 min VSA. Unannealed samples were composed of a uniform, amorphous MeDPP film (0.5–0.6 nm) with a few MeDPP aggregates (~8 nm) on the top of the film, while annealed films coalesce into similarly sized aggregates (Figure S9), again suggesting that amorphous MeDPP is converted into crystalline aggregates by VSA. STS measurements show 60 min VSA films have max conductivity when positively biased while unannealed films show max conductivity when negatively biased (Figure S10). This indicates the change in the alignment of the frontier orbitals to a stronger $\pi\cdots\pi$ interaction that occurs upon crystallite formation, which shift the transport through LUMO more favorably at a positive tip bias. The relative *H*:*J* composition of the films were estimated (Figure S7 & S8) by assuming the 60 min VSA films possessed exclusively *J*-aggregates. This is supported by the fact that there is no detectable *H*-aggregate GIWAXS signal in 60 min VSA films, whereas all films exposed to CH_2Cl_2 vapor were composed of only *H*- and *J*-aggregates (Figure 3 bottom, S7, and S8).

Femtosecond (fs) and nanosecond (ns) TA spectroscopy were used to probe the SF dynamics and triplet yields in MeDPP films with different VSA times. For fs-TA measurements, films were excited at 500 nm under low fluence conditions (35 μJ/cm^2) that minimize the singlet-singlet exciton annihilation (Figures S17 and S18), yielding a total excitation density on the order of 10^{18} cm^{-3}. For ns-TA measurements, the excitation density was increased to ~ 10^{19} cm^{-3} to obtain larger triplet signals at long time scales. The $^1(T_1T_1)$ and (T_1) lifetimes were determined from global analysis of the ns-TA data. Representative data for the as-deposited and annealed (60 min) films are shown in Figure 4, while data from other VSA time films are given in Figure S12.

Results and Discussion

TA spectra show a broad excited state absorption (ESA) for wavelengths longer than 620 nm, which is assigned to the singlet state (Figures 4A and 4B). For as-deposited films of MeDPP, the ground state bleach (GSB) consists of a feature that matches the steady

state absorption at around 570 nm, and an additional red-shifted peak that we assign to stimulated emission. In as-deposited films, the broad ESA of singlet state (S_1^*) cools within 1.6 ± 0.2 ps to a relaxed singlet state (S_1) (red trace in Figure 4C), followed by $^1(T_1T_1)$ formation in 30.6 ± 0.2 ps. A net blue-shift occurs for the GSB features during the singlet state cooling process, corresponding to the loss of stimulated emission. The triplet signal is characterized by a positive excited state absorption signal near 550 nm that overlaps with the negative GSB feature and decays on much longer time scales. The triplet state is assigned by comparison to the triplet state generated by sensitization experiments in the spin-coated films (Figure S14). For annealed films, a three-state kinetic model was also used to fit the TA data (Figure 4D). Here, for 60 min VSA film, the (S_1^*) cools in 1.7 ± 0.1 ps and $^1(T_1T_1)$ forms in 23.3 ± 0.6 ps, in agreement with previous reports.[22] Similar to the as-deposited film, an obvious blue-shift of the GSB from 595 nm to 585 nm is observed in the 60 min VSA film during the cooling process, while other features (e.g. at 540 nm) remain constant. We observe some enhancement of the singlet excited state absorption in the NIR region, suggesting a slightly different morphology than was previously observed.[22] For all annealed films, $^1(T_1T_1)$ forms in the timescale 22–24 ps, faster than the as-deposited film, indicating that the annealing process forms polymorphs that favor SF.

The decay of $^1(T_1T_1)$ and (T_1) are determined using ns-TA measurements. Based on the global analysis (Figure S11 and S13), the triplet decay was decomposed into a fast (~50 ns) and a slow (~500 ns) component, which can be attributed to the $^1(T_1T_1)$-to-(T_1) and (T_1) decay, respectively. The $^1(T_1T_1)$ yields of all the films are shown in Figure 3, which are determined by the modified ground state bleach method described previously (details in SI).[22, 30, 43] Based on this methodology, we separately obtain the quantum yield of the $^1(T_1T_1)$ and (T_1) (Figure 3). $^1(T_1T_1)$ yield from SF of the unannealed film is lower, around 90%, and then plateaus at ~100% for all the annealed MeDPP films (Figure 3 top). Given the conversion of amorphous material to *H/J* in the first minute, these data imply that both *J*- and *H*- aggregates are efficient in $^1(T_1T_1)$ generation, the first step of SF.

In contrast, the (T_1) yields exhibit a notable increase with increasing VSA time until plateauing near 15 min VSA (Figure 3 middle). The initial increase in the first minute may be explained by conversion of any amorphous MeDPP to the *H/J* mixture, but the continued increase after one minute, given the growing proportion of *J*-aggregates, implies that *J*-aggregates are more efficient at decoupling triplets. This can be explained by the difference in V_{ST} values between the nearest neighbors obtained through modeling (Figure S19) because *H*-aggregates (157.56 meV) couple more strongly than *J*-aggregates (59.51 meV). Both types of aggregates possess adequate V_{ST} to promote efficient SF to form $^1(T_1T_1)$, but the lower value of V_{ST} for *J*-aggregate allows more efficient decoupling to form (T_1), with yields as high as 106%.

Conclusion

Upon VSA, MeDPP films composed of multiple polymorphs were converted to predominantly *J*-aggregates. Though both *H*- and *J*-aggregates comparably and efficiently form $^1(T_1T_1)$ via SF, the lower V_{ST} of *J*-aggregate relative to the *H*-aggregate results in higher (T_1) yields. By comparing SF dynamics in polymorphs of the same material, these

studies provide a more complete understanding of the subtle structure-activity relationships that drive efficient (T_1) generation, which could lead the way to more efficient photovoltaics that incorporate SF dyes as sensitizers.

Supplementary Material

Refer to Web version on PubMed Central for supplementary material.

ACKNOWLEDGMENT

REFERENCES

1. Shockley W; Queisser HJ, Detailed Balance Limit of Efficiency of p-n Junction Solar Cells. Journal of Applied Physics 1961, 32, 510–519.

2. Nielsen CB; Turbiez M; McCulloch I, Recent Advances in the Development of Semiconducting DPP-Containing Polymers for Transistor Applications. Advanced Materials 2013, 25, 1859–1880. [PubMed: 23008141]

3. Lee J; Jadhav P; Reusswig PD; Yost SR; Thompson NJ; Congreve DN; Hontz E; Van Voorhis T; Baldo MA, Singlet Exciton Fission Photovoltaics. Accounts of Chemical Research 2013, 46, 1300–1311. [PubMed: 23611026]

4. Smith MB; Michl J, Recent Advances in Singlet Fission. Annual Review of Physical Chemistry 2013, 64, 361–386.

5. Einzinger M; Wu T; Kompalla JF; Smith HL; Perkinson CF; Nienhaus L; Wieghold S; Congreve DN; Kahn A; Bawendi MG, et al. , Sensitization of silicon by singlet exciton fission in tetracene. Nature 2019, 571, 90–94. [PubMed: 31270480]

6. Daiber B; Pujari SP; Verboom S; Luxembourg SL; Tabernig SW; Futscher MH; Lee J; Zuilhof H; Ehrler B, A method to detect triplet exciton transfer from singlet fission materials into silicon solar cells: Comparing different surface treatments. The Journal of Chemical Physics 2020, 152, 114201. [PubMed: 32199443]

7. Wu TC; Thompson NJ; Congreve DN; Hontz E; Yost SR; Voorhis TV; Baldo MA, Singlet fission efficiency in tetracene-based organic solar cells. Applied Physics Letters 2014, 104, 193901.

8. Biswas S; Kumar M; Levine AM; Jimenez I; Ulijn RV; Braunschweig AB, Visible-light photooxidation in water by 1O2-generating supramolecular hydrogels. Chemical Science 2020, 11, 4239–4245.

9. Kumarasamy E; Sanders SN; Tayebjee MJY; Asadpoordarvish A; Hele TJH; Fuemmeler EG; Pun AB; Yablon LM; Low JZ; Paley DW, et al. , Tuning Singlet Fission in π-Bridge-π Chromophores. Journal of the American Chemical Society 2017, 139, 12488–12494. [PubMed: 28799752]

10. Young RM; Wasielewski MR, Mixed Electronic States in Molecular Dimers: Connecting Singlet Fission, Excimer Formation, and Symmetry-Breaking Charge Transfer. Accounts of Chemical Research 2020, 53, 1957–1968. [PubMed: 32786248]

11. Basel BS; Zirzlmeier J; Hetzer C; Phelan BT; Krzyaniak MD; Reddy SR; Coto PB; Horwitz NE; Young RM; White FJ, et al. , Unified model for singlet fission within a non-conjugated covalent pentacene dimer. Nature Communications 2017, 8, 15171.

12. Margulies EA; Miller CE; Wu Y; Ma L; Schatz GC; Young RM; Wasielewski MR, Enabling singlet fission by controlling intramolecular charge transfer in π-stacked covalent terrylenediimide dimers. Nature Chemistry 2016, 8, 1120–1125.

13. Chen M; Bae YJ; Mauck CM; Mandal A; Young RM; Wasielewski MR, Singlet Fission in Covalent Terrylenediimide Dimers: Probing the Nature of the Multiexciton State Using Femtosecond Mid-Infrared Spectroscopy. Journal of the American Chemical Society 2018, 140, 9184–9192. [PubMed: 29949371]

14. Huang H; He G; Xu K; Wu Q; Wu D; Sfeir MY; Xia J, Achieving Long-Lived Triplet States in Intramolecular SF Films through Molecular Engineering. Chem 2019, 5, 2405–2417.

15. Pun AB; Asadpoordarvish A; Kumarasamy E; Tayebjee MJY; Niesner D; McCamey DR; Sanders SN; Campos LM; Sfeir MY, Ultra-fast intramolecular singlet fission to persistent multiexcitons by molecular design. Nature Chemistry 2019, 11, 821–828.

16. Korovina NV; Chang CH; Johnson JC, Spatial separation of triplet excitons drives endothermic singlet fission. Nature Chemistry 2020, 12, 391–398.

17. Bayliss SL; Weiss LR; Rao A; Friend RH; Chepelianskii AD; Greenham NC, Spin signatures of exchange-coupled triplet pairs formed by singlet fission. Physical Review B 2016, 94, 045204.

18. Arias DH; Ryerson JL; Cook JD; Damrauer NH; Johnson JC, Polymorphism influences singlet fission rates in tetracene thin films. Chemical Science 2016, 7, 1185–1191. [PubMed: 29910873]

19. Grieco C; Doucette GS; Munro JM; Kennehan ER; Lee Y; Rimshaw A; Payne MM; Wonderling N; Anthony JE; Dabo I, et al. , Triplet Transfer Mediates Triplet Pair Separation during Singlet Fission in 6,13-Bis(triisopropylsilylethynyl)-Pentacene. Advanced Functional Materials 2017, 27, 1703929.

20. Miller CE; Wasielewski MR; Schatz GC, Modeling Singlet Fission in Rylene and Diketopyrrolopyrrole Derivatives: The Role of the Charge Transfer State in Superexchange and Excimer Formation. The Journal of Physical Chemistry C 2017, 121, 10345–10350.

21. Ryerson JL; Schrauben JN; Ferguson AJ; Sahoo SC; Naumov P; Havlas Z; Michl J; Nozik AJ; Johnson JC, Two Thin Film Polymorphs of the Singlet Fission Compound 1,3-Diphenylisobenzofuran. The Journal of Physical Chemistry C 2014, 118, 12121–12132.

22. Mauck CM; Hartnett PE; Margulies EA; Ma L; Miller CE; Schatz GC; Marks TJ; Wasielewski MR, Singlet Fission via an Excimer-Like Intermediate in 3,6-Bis(thiophen-2-yl)diketopyrrolopyrrole Derivatives. Journal of the American Chemical Society 2016, 138, 11749–11761. [PubMed: 27547986]

23. Rais D; Toman P; Pfleger J; Acharya U; Panthi YR; Menšík M; Zhigunov A; Thottappali MA; Vala M; Marková A, et al. , Singlet Fission in Thin Solid Films of Bis(thienyl)diketopyrrolopyrroles. ChemPlusChem 2020, 85, 2689–2703. [PubMed: 33332757]

24. Tang A; Zhan C; Yao J; Zhou E, Design of Diketopyrrolopyrrole (DPP)-Based Small Molecules for Organic-Solar-Cell Applications. Advanced Materials 2017, 29, 1600013.

25. Chandran D; Lee K-S, Diketopyrrolopyrrole: A versatile building block for organic photovoltaic materials. Macromolecular Research 2013, 21, 272–283.

26. Li Y; Sonar P; Murphy L; Hong W, High mobility diketopyrrolopyrrole (DPP)-based organic semiconductor materials for organic thin film transistors and photovoltaics. Energy & Environmental Science 2013, 6, 1684–1710.

27. Li W; Hendriks KH; Wienk MM; Janssen RAJ, Diketopyrrolopyrrole Polymers for Organic Solar Cells. Accounts of Chemical Research 2016, 49, 78–85. [PubMed: 26693798]

28. Wu Y; Zhu W, Organic sensitizers from D–π–A to D–A–π–A: effect of the internal electron-withdrawing units on molecular absorption, energy levels and photovoltaic performances. Chemical Society Reviews 2013, 42, 2039–2058. [PubMed: 23192709]

29. Bao WW; Li R; Dai ZC; Tang J; Shi X; Geng JT; Deng ZF; Hua J, Diketopyrrolopyrrole (DPP)-Based Materials and Its Applications: A Review. Frontiers in Chemistry 2020, 8. [PubMed: 32039163]

30. Levine AM; Schierl C; Basel BS; Ahmed M; Camargo BA; Guldi DM; Braunschweig AB, Singlet Fission in Combinatorial Diketopyrrolopyrrole–Rylene Supramolecular Films. The Journal of Physical Chemistry C 2019, 123, 1587–1595.

31. Casillas R; Papadopoulos I; Ullrich T; Thiel D; Kunzmann A; Guldi DM, Molecular insights and concepts to engineer singlet fission energy conversion devices. Energy & Environmental Science 2020, 13, 2741–2804.

32. Karsten BP; Bouwer RKM; Hummelen JC; Williams RM; Janssen RAJ, Charge separation and (triplet) recombination in diketopyrrolopyrrole–fullerene triads. Photochemical & Photobiological Sciences 2010, 9, 1055–1065. [PubMed: 20532279]

33. Guzman CX; Calderon RMK; Li Z; Yamazaki S; Peurifoy SR; Guo C; Davidowski SK; Mazza MMA; Han X; Holland G, et al. , Extended Charge Carrier Lifetimes in Hierarchical Donor–Acceptor Supramolecular Polymer Films. The Journal of Physical Chemistry C 2015, 119, 19584–19589.

34. Nannenga BL; Gonen T, The cryo-EM method microcrystal electron diffraction (MicroED). Nature Methods 2019, 16, 369–379. [PubMed: 31040436]

35. Nannenga BL; Shi D; Hattne J; Reyes FE; Gonen T, Structure of catalase determined by MicroED. Elife 2014, 3, e03600. [PubMed: 25303172]

36. Shi D; Nannenga BL; Iadanza MG; Gonen T, Three-dimensional electron crystallography of protein microcrystals. Elife 2013, 2, e01345. [PubMed: 24252878]

37. Nannenga BL, MicroED methodology and development. Structural Dynamics 2020, 7, 014304.

38. Levine AM; Bu G; Biswas S; Tsai EHR; Braunschweig AB; Nannenga BL, Crystal structure and orientation of organic semiconductor thin films by microcrystal electron diffraction and grazing-incidence wide-angle X-ray scattering. Chemical Communications 2020, 56, 4204–4207. [PubMed: 32167510]

39. Kirkus M; Wang L; Mothy S; Beljonne D; Cornil J; Janssen RAJ; Meskers SCJ, Optical Properties of Oligothiophene Substituted Diketopyrrolopyrrole Derivatives in the Solid Phase: Joint J- and H-Type Aggregation. The Journal of Physical Chemistry A 2012, 116, 7927–7936. [PubMed: 22757695]

40. Más-Montoya M; Janssen RAJ, The Effect of H- and J-Aggregation on the Photophysical and Photovoltaic Properties of Small Thiophene–Pyridine–DPP Molecules for Bulk-Heterojunction Solar Cells. Advanced Functional Materials 2017, 27, 1605779.

41. Wagner W; Wehner M; Stepanenko V; Ogi S; Würthner F, Living Supramolecular Polymerization of a Perylene Bisimide Dye into Fluorescent J-Aggregates. Angewandte Chemie International Edition 2017, 56, 16008–16012. [PubMed: 29035005]

42. Zhou Y; Guzman CX; Helguero-Kelley LC; Liu C; Peurifoy SR; Captain B; Braunschweig AB, Diketopyrrolopyrrole assembly into J-aggregates. Journal of Physical Organic Chemistry 2016, 29, 689–699.

43. Carmichael I; Hug GL, Triplet–Triplet Absorption Spectra of Organic Molecules in Condensed Phases. Journal of Physical and Chemical Reference Data 1986, 15, 1–250.
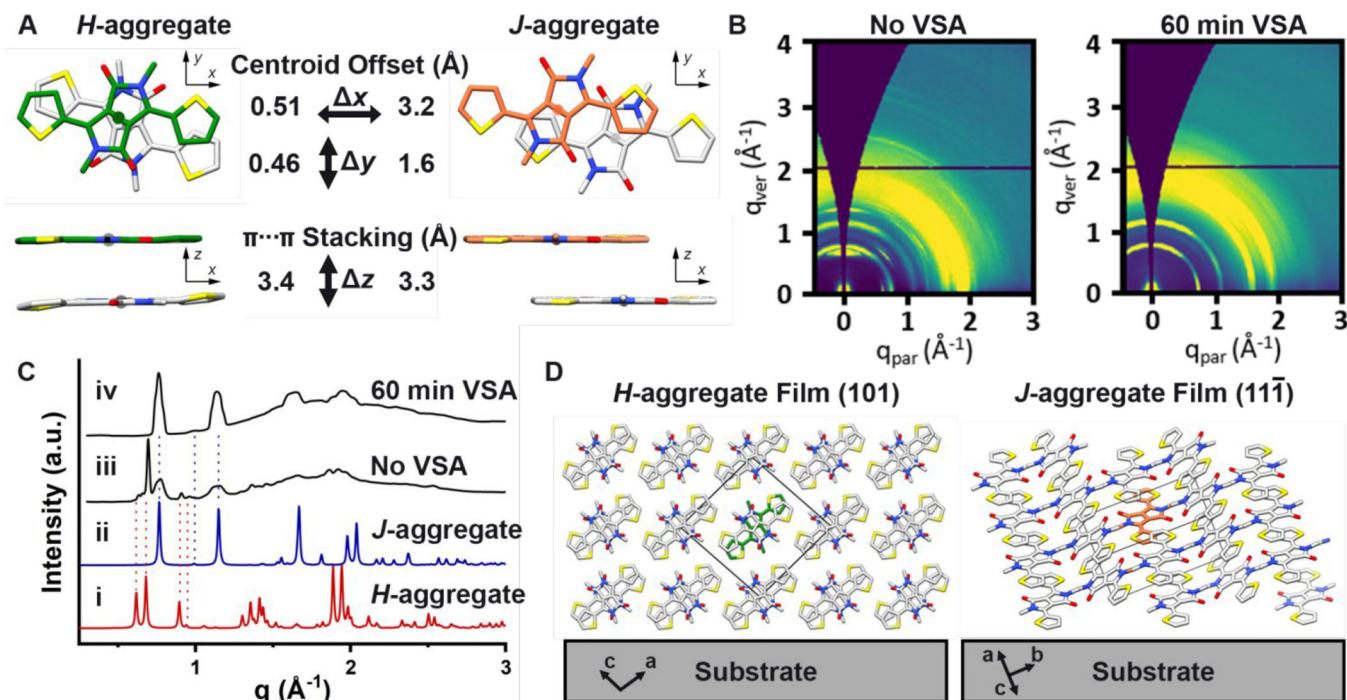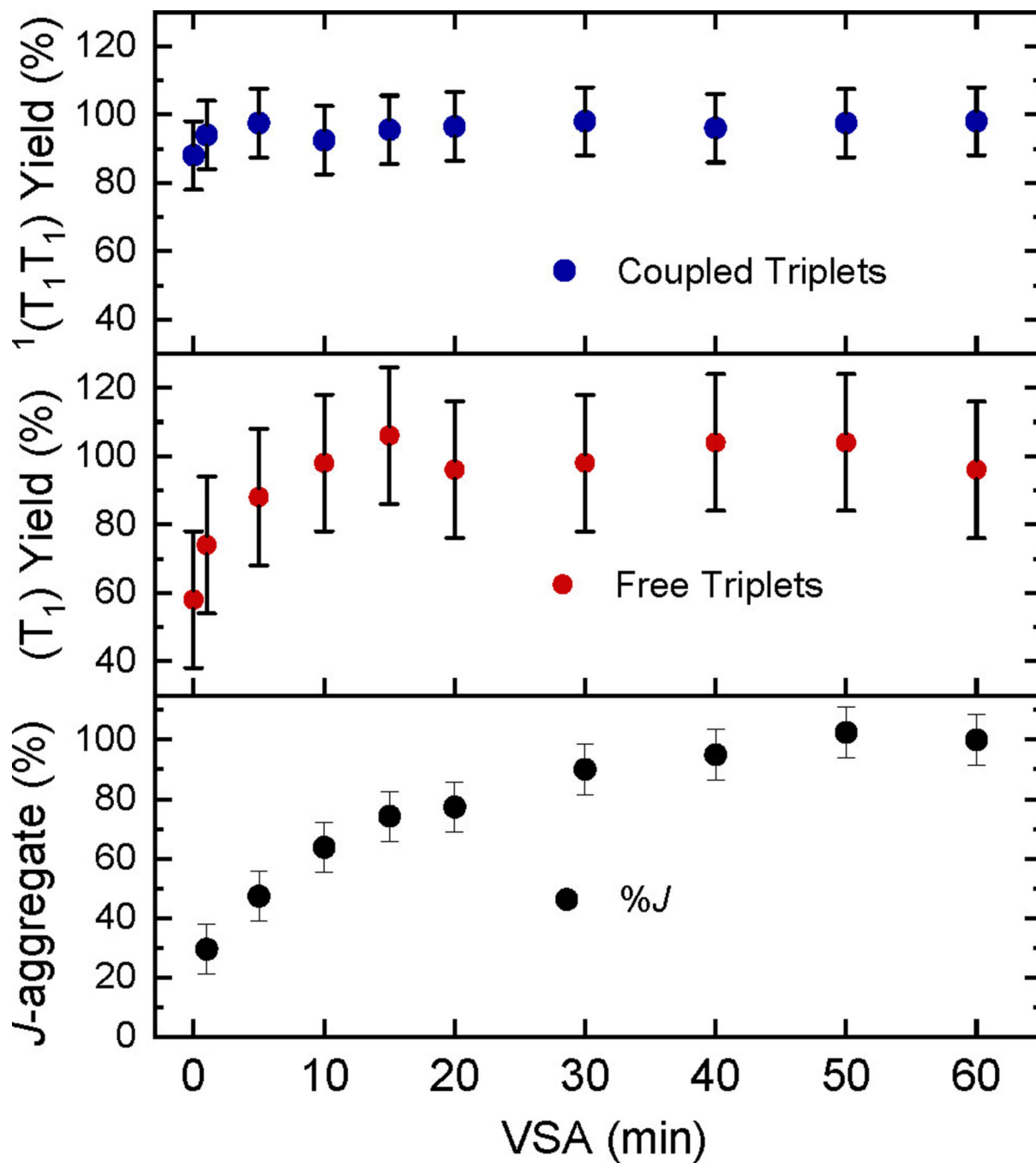
Figure 1.
(A) MicroED determined crystal structures for *H*- and *J*-aggregate MeDPP (Atom colors: *H*-aggregate C, grey or green; *J*-aggregate C, grey or orange; N, blue; O, red.; S, sulfur). (B) GIWAXS scattering pattern of thermally evaporated MeDPP films before and after vapor solvent annealing (VSA) in CH_2Cl_2. (C) Comparison of calculated powder patterns from MicroED solved *H*- (i) and *J*- (ii) aggregates with GIWAXS 1D integrated intensity of thin films without (iii) and with (iv) VSA. (D) MeDPP unit cell packing of *H*- and *J*-aggregates depicted as they are oriented with respect to substrate surface normal.
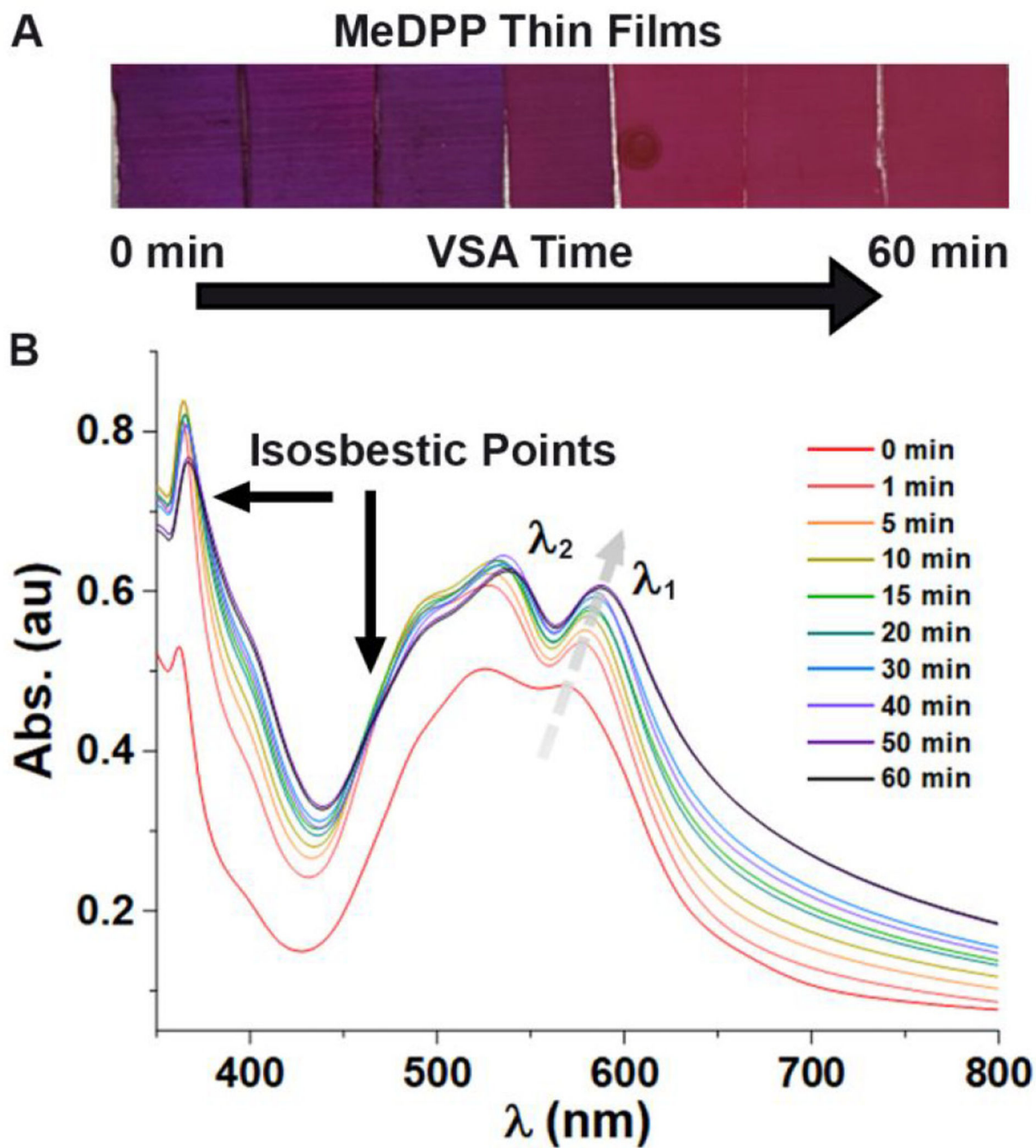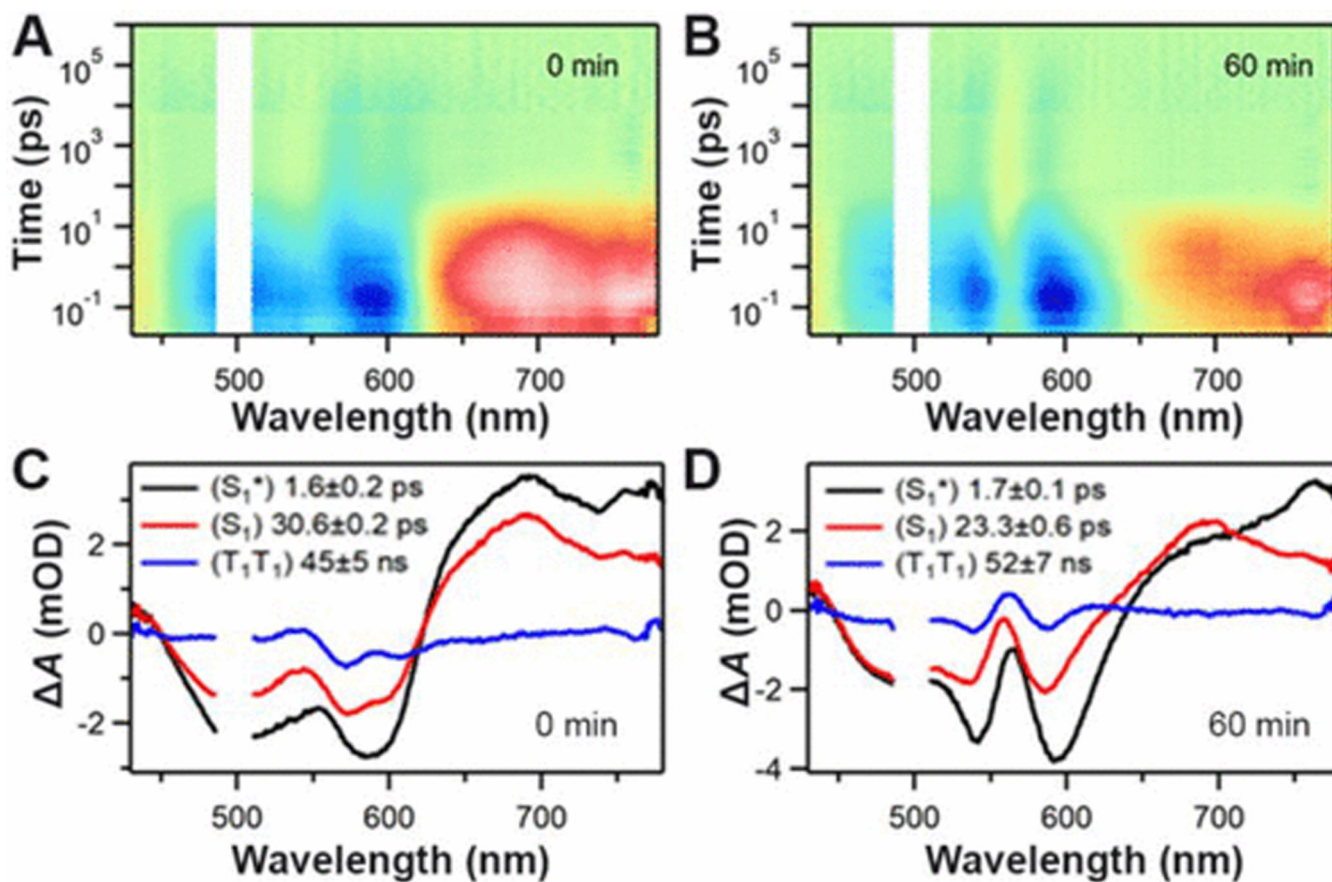
Figure 2.
(A) Optical images of films MeDPP (216 ± 18 nm) as they are exposed to CH_2Cl_2 vapor for different times. (B) UV-Vis absorption spectra of MeDPP films with exposure to CH_2Cl_2 vapor for different times.

Figure 3.
Correlating SF efficiencies to %*J*-aggregation in VSA thin films. (Bottom) %*J* composition, (middle) free triplet (T_1) quantum yields, and (top) coupled triplet $^1(T_1T_1)$ quantum yields as a function of VSA time.

Figure 4.
(A) Fs- and ns-TA of as-deposited MeDPP film, (B) fs- and ns-TA of 60 min VSA MeDPP film, (C) global analysis of fs-TA data for as-deposited MeDPP film, and (D) global analysis of fs-TA data for 60 min VSA MeDPP film. Fs-TA kinetics from global analyses are shown as singlet state (S_1^*) (black), relaxed singlet state (S_1) (red), and coupled triplet state $^1(T_1T_1)$ (blue).